Designing Energy-Minimizing Rigid Body Motions in the Presence of Obstacles

Michael Hofer [a,*], Helmut Pottmann [a],

[a]*Research Group 'Geometric Modeling and Industrial Geometry'*
Vienna University of Technology
Wiedner Hauptstr. 8-10, A-1040 Wien, Austria

Abstract

We present a solution for variational motion design of a rigid body in the presence of rigid obstacles of arbitrary shape that fully employs the available degrees of freedom in the design process. This question remained open in our paper on energy-minimizing splines in manifolds (Hofer and Pottmann, 2004). The main idea is to reduce the problem to a curve design task on a suitable barrier surface embedded in an appropriate kinematic image space.

Key words: motion design, obstacles, optimization, variational approach.

1 Introduction

1.1 Previous Work

Motion design (path planning) in the presence of obstacles is a well-studied problem in Computational Geometry and Robotics (de Berg et al., 2000; Choset et al., 2005; Latombe, 2001). The classical 'piano mover's problem' deals with the task of generating a collision-free path among known rigid obstacles from a starting position to a given end position of the piano.

---

* Corresponding author.
   Email addresses: `hofer@geometrie.tuwien.ac.at` (Michael Hofer),
`pottmann@geometrie.tuwien.ac.at` (Helmut Pottmann).
   URLs: `http://www.geometrie.tuwien.ac.at/hofer` (Michael Hofer),
`http://www.geometrie.tuwien.ac.at/pottmann` (Helmut Pottmann).

Our approach is inspired by the literature on motion design in Computer Aided Geometric Design and Kinematics. This area of research started with the seminal paper by Shoemake (1985) and lead to many contributions, see the survey article by Jüttler and Wagner (2002). Variational motion design — without consideration of obstacles — has been studied e.g. by Barr et al. (1992) and Ramamoorthi and Barr (1997).

The problem of designing a smooth rigid body motion in Euclidean 3-space can be solved by computing a smooth curve in a kinematic image space. It is interesting to note that there are only a few contributions in the literature that deal with the problem of designing smooth curves in the presence of obstacles. We point to work on interpolation with cubic spline functions under linear inequality constraints (Opfer and Oberle, 1988), CAD related work on constrained curve design without energy minimization (Meek et al., 2003), and in particular to Bohl's contribution to splines on (trimmed) parametric surfaces (Bohl, 1999). A recent contribution by Myles and Peters (2005) is an algorithm for generating a parametric spline curve with few pieces that traverses a polygonal channel between obstacles. They solve a linear feasibility problem by standard linear programming techniques.

We will see later that we can get rid of the obstacle constraints by introducing an appropriate unbounded auxiliary surface $M_{\mathcal{B}}$ in the kinematic image space. The obstacle avoiding smooth rigid body motion is then computed as a smooth curve on $M_{\mathcal{B}}$. Recent work by Azariadis and Aspragathos (2005) uses a similar idea of representing the whole environment including the obstacles as one single surface, labeled 'Bump-surface' by the authors. However, in their approach the moving body is only a single point.

Our own previous work (Hofer and Pottmann, 2004) contributed to motion design a new metric in the kinematic image space and an optimization algorithm for variational motion design. We also presented a conservative solution for motion design in the presence of obstacles.

1.2   Contributions of the Present Paper

The main contribution of the present paper is an algorithm that fully employs all available degrees of freedom to solve the task of computing a smooth energy-minimizing rigid body motion in the presence of obstacles. Thus we answer a question that remained open in our paper (Hofer and Pottmann, 2004). In Section 2 we review the kinematic image space, the energy-functionals, and the basic geometric optimization algorithm we will use. Section 3 presents the new contribution and Section 4 is used for examples and discussion.
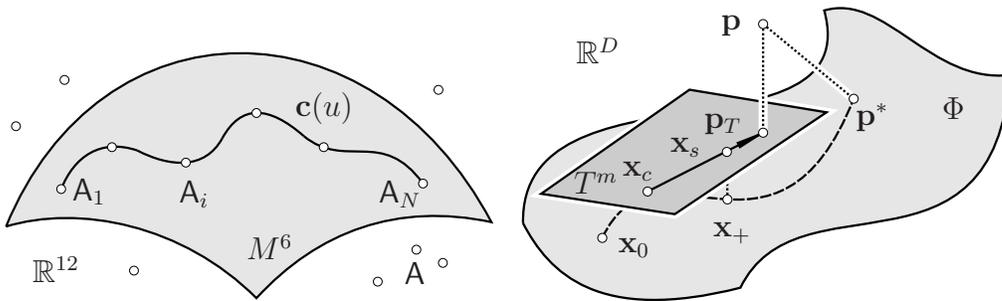
Fig. 1. (Left) The kinematic image space. (Right) The geometric optimization algorithm.

2 Setting and Techniques

2.1 The Kinematic Image Space

We use the kinematic image space as introduced in Hofer and Pottmann (2004). Consider two Cartesian coordinate systems, the fixed one Σ whose points are denoted by $\mathbf{x}, \mathbf{y}$, and the moving one Σ^0 with points $\mathbf{x}^0, \mathbf{y}^0$ and so forth. An affine map α maps a point $\mathbf{x}^0 = (x_1^0, x_2^0, x_3^0)$ of Σ^0 to the point $\mathbf{x}$ of Σ as follows,

$$\mathbf{x} = \alpha(\mathbf{x}^0) = \mathbf{a}_0 + \mathbf{A} \cdot \mathbf{x}^0 = \mathbf{a}_0 + x_1^0 \mathbf{a}_1 + x_2^0 \mathbf{a}_2 + x_3^0 \mathbf{a}_3.$$

The translational part of the affine map α is $\mathbf{a}_0 \in \mathbb{R}^3$ and the linear part of α is given by the matrix $\mathbf{A} := [\mathbf{a}_1, \mathbf{a}_2, \mathbf{a}_3] \in \mathbb{R}^{3\times3}$. We define the kinematic image space in the following way (see Fig. 1, left): With each affine map α we associate a point in 12-dimensional space $\mathbb{R}^{12}$, represented by the vector $\mathsf{A} := (\mathbf{a}_0, \ldots, \mathbf{a}_3)$. The images of Euclidean maps $\alpha \in SE(3)$ form a 6-dimensional manifold $M^6 \subset \mathbb{R}^{12}$. Its 6 equations are given by the orthogonality conditions of the matrix $\mathbf{A}$, i.e., $\mathbf{a}_i \cdot \mathbf{a}_j = \delta_{ij}$ for $i, j = 1, 2, 3$ and δ_{ij} is the Kronecker delta. A *one-parameter rigid body motion* $\mathcal{B}(u)$ in $\mathbb{R}^3$ is a smooth family of Euclidean congruence transformations and corresponds to a curve $\mathbf{c}(u) \subset M^6$ in the kinematic image space, see Fig. 1, left.

For distance computations in $\mathbb{R}^{12}$ we use the *metric* defined in Hofer and Pottmann (2004) that is based on a point set $\mathbf{x}_1^0, \mathbf{x}_2^0, \ldots, \mathbf{x}_K^0$ spread over the rigid body $\mathcal{B}$. Let the coordinate system Σ^0 be such that the barycenter of $\mathcal{B}$ is the origin and the eigenvectors of the inertia tensor $\mathbf{J} := \sum_i \mathbf{x}_i^0 \cdot \mathbf{x}_i^{0T}$ are the coordinate axes. Then the six vertices of $\mathcal{B}'s$ inertia ellipsoid have the coordinates $(\pm f_1, 0, 0), (0, \pm f_2, 0), (0, 0, \pm f_3)$ where $2f_i^2$ are the eigenvalues of $\mathbf{J}$. Now we define the squared distance between two affine maps α and β as the sum of squared distances between corresponding point positions and see

3

that it only depends on the barycenter and inertia tensor,

$$\|\alpha - \beta\|^2 := \sum_{i=1}^{K} \|\alpha(\mathbf{x}_i^0) - \beta(\mathbf{x}_i^0)\|^2 = 6(\mathbf{a}_0 - \mathbf{b}_0)^2 + 2\sum_{i=1}^{3} f_i^2(\mathbf{a}_i - \mathbf{b}_i)^2.$$

Thereby $\mathsf{A} = (\mathbf{a}_0, \ldots, \mathbf{a}_3)$ and $\mathsf{B} = (\mathbf{b}_0, \ldots, \mathbf{b}_3)$ are the kinematic image points of the affine maps α and β.

Using the above kinematic image space we reduce our motion design problem to a curve design problem on a certain surface. Since we deal with variational design we will first introduce the energy functionals we are working with in Section 2.2. Section 2.3 recalls the geometric optimization algorithm of Hofer and Pottmann (2004) to compute an energy-minimizing curve on a surface of arbitrary dimension and codimension. Finally, in Section 3 we specifically address the design of energy-minimizing rigid body motions in the presence of obstacles that employs all available degrees of freedom.

2.2   The Energy Functionals

Let S be a k-dimensional regular surface, embedded in Euclidean space $\mathbb{R}^n$, $k < n$. Given are N points $\mathbf{p}_1, \ldots, \mathbf{p}_N \in S$ and corresponding parameters $u_1, \ldots, u_N$. We are seeking an interpolating curve $\mathbf{c}(u)$ on S with $\mathbf{c}(u_i) = \mathbf{p}_i$ that minimizes one of the following energy functionals,

$$E_1(\mathbf{x}) = \int_{u_1}^{u_N} \|\dot{\mathbf{x}}(u)\|^2 du, \quad E_2(\mathbf{x}) = \int_{u_1}^{u_N} \|\ddot{\mathbf{x}}(u)\|^2 du, \quad E_\tau = E_2 + \tau E_1.$$

The minimizer of E_1 is a *geodesic* on S traced with constant speed. As shown in Hofer and Pottmann (2004), the minimizers of E_2 and E_τ are surface counterparts to *cubic splines* and *splines in tension*, respectively. For the numerical solution we discretize the energy-functionals (using a Newton-Cotes formula) to get quadratic functions that have to be minimized under the constraint that the curves are restricted to a surface S. For this purpose we use the geometric optimization algorithm of Hofer and Pottmann (2004), which we summarize below.

2.3   The Geometric Optimization Algorithm

The following algorithm computes an energy-minimizing spline curve on a surface of arbitrary dimension and codimension. A more detailed discussion including a convergence analysis can be found in Hofer and Pottmann (2004).

Algorithm 1 (The geometric optimization algorithm) *We compute the minimizer $\mathbf{p}^*$ of a quadratic function F,*

$$F : \mathbb{R}^D \to \mathbb{R}, \quad F(\mathbf{x}) = (\mathbf{x} - \mathbf{p})^T \cdot \mathbf{Q} \cdot (\mathbf{x} - \mathbf{p}),$$

under the constraint that $\mathbf{p}^*$ lies on a given m-dimensional surface $\Phi \subset \mathbb{R}^D$. The value of $F(\mathbf{x})$ is the squared distance $\|\mathbf{x} - \mathbf{p}\|^2$ of the point $\mathbf{x}$ to the unconstrained minimizer $\mathbf{p}$ of F in the Euclidean metric with inner product $\langle \mathbf{x}, \mathbf{y} \rangle := \mathbf{x}^T \cdot \mathbf{Q} \cdot \mathbf{y}$ given by the positive definite matrix $\mathbf{Q}$. Starting with an initial guess $\mathbf{x}_c = \mathbf{x}_0$, we compute the constrained minimizer $\mathbf{p}^* \in \Phi$ by iteratively applying the following two steps (see Fig. 1, right):

(1) *Compute a basis $\{\mathbf{c}_1, \ldots, \mathbf{c}_m\}$ of $\Phi's$ tangent space T^m at the current iterate $\mathbf{x}_c$, and it's Gramian matrix $\mathbf{G} = (g_{ij}) = (\langle \mathbf{c}_i, \mathbf{c}_j \rangle) = (\mathbf{c}_i^T \cdot \mathbf{Q} \cdot \mathbf{c}_j)$. Further compute the vector $\mathbf{r} := (r_1, \ldots, r_m)$ where $r_j := \langle \mathbf{p} - \mathbf{x}_c, \mathbf{c}_j \rangle$. The solution $\mathbf{v} = (v_1, \ldots, v_m)$ of the linear system $\mathbf{G} \cdot \mathbf{v} = \mathbf{r}$ defines the tangent vector $\mathbf{t} := \sum_i v_i \mathbf{c}_i$ at $\mathbf{x}_c$. Note that the point $\mathbf{p}_T := \mathbf{x}_c + \mathbf{t}$ is the normal projection of $\mathbf{p}$ onto T^m.*

(2) *Compute an appropriate step size s (see Hofer and Pottmann (2004) for details) and project $\mathbf{x}_s := \mathbf{x}_c + s\mathbf{t}$ onto Φ to get the next iterate $\mathbf{x}_+$.*

3 Variational Motion Design in the Presence of Obstacles

In Hofer and Pottmann (2004) we have described how to compute an energy-minimizing rigid body motion where the moving body $\mathcal{B}$ avoids given obstacles via a single enclosing ball $\mathcal{B}_e$. The enclosing ball $\mathcal{B}_e$ itself avoids the obstacles; since it is centered in the barycenter of $\mathcal{B}$, the problem can be split into the computation of the trajectory of the ball's center and the computation of the rotational part. Only the first part of the computation needs to consider the obstacles. This approach is rather conservative and does not fully exploit the available degrees of freedom.

In the present paper we capture the shape of the moving body $\mathcal{B}$ more precisely. For the theoretic considerations we consider the moving body $\mathcal{B}$ and the obstacle $\mathcal{O}$ to be smooth solid bodies.

3.1 Definition of the Barrier Manifold

The moving body $\mathcal{B}$ is a solid. A position $\alpha(\mathcal{B})$ of the body corresponds to some displacement α, seen as a point A in M^6. In the following, we speak of a single obstacle $\mathcal{O}$, but note that it may contain several components. For simplicity, we assume right now that both $\mathcal{B}$ and $\mathcal{O}$ have smooth boundary
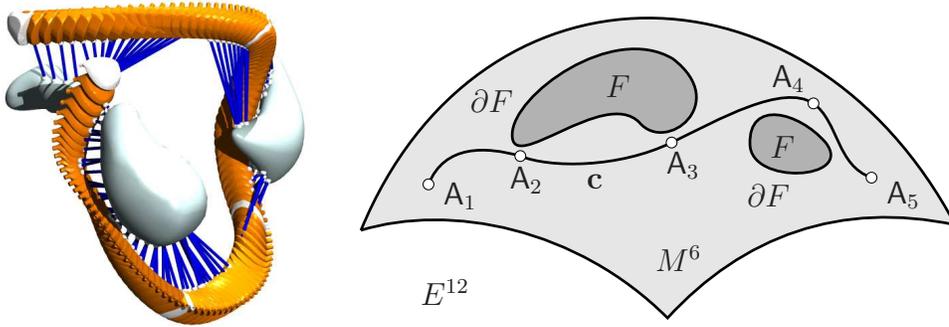
Fig. 2. (Left) Rigid body motion $\mathcal{B}(u)$ in $\mathbb{R}^3$ interpolating 5 given positions with shortest distances to the obstacles. (Right) Forbidden region F and the curve $\mathbf{c}$ corresponding to $\mathcal{B}(u)$ on the manifold $M^6 \subset E^{12}$.

surfaces. In our implementation we use triangle meshes to represent both, $\mathcal{B}$ and $\mathcal{O}$.

Those positions $\alpha(\mathcal{B})$, which penetrate $\mathcal{O}$, have to be avoided. One may view these forbidden positions as points in some subset F of M^6, see Fig. 2. Like $\mathcal{O}$, it may have several components. In order to stay away from F, we build a barrier manifold against it, according to the concept presented in Hofer and Pottmann (2004) for the curve case, see Fig. 3. To do so, we use a *distance function d*. The distance $d(\alpha) = d(\mathsf{A}) =: d_0$ is the shortest distance between the corresponding position $\alpha(\mathcal{B})$ of $\mathcal{B}$ and the obstacle $\mathcal{O}$, see Fig. 2 (left) and Fig. 4. Note that we view d as a function defined on M^6.

In case of penetration, we define $d(\mathsf{A}) = -1$. Of special interest is the zero level set of d, since it is the boundary ∂F of F. It contains exactly those positions in which $\alpha(\mathcal{B})$ is tangent to $\mathcal{O}$, but not penetrating the obstacle. Likewise, any other level set to a constant distance value d_0 contains the positions, where $\alpha(\mathcal{B})$ is in contact with the offset $\tilde{\mathcal{O}}$ of $\mathcal{O}$ at distance d_0, see Fig. 4.

We use a function $f(d)$ (blending profile function) which is supported on some interval $[0, D]$. It describes a smooth blend between f-axis and d-axis, and thus it has a positive value h and infinite derivative at 0, and satisfies $f(D) = f'(D) = 0$, see Fig. 3.

The barrier manifold $M_{\mathcal{B}}$ is a 6-dimensional manifold, embedded in $\mathbb{R}^{13}$. Part of it can be parameterized over M^6: If $d(\mathsf{A}) > 0$, the corresponding point on $M_{\mathcal{B}}$ is $(\mathsf{A}, f(d(\mathsf{A})))$. This surface contains a part in M^6 (for $d \geq D$), and a blending part which reaches height h in the 13-th coordinate, when A reaches the boundary ∂F of the forbidden region F. There, the surface is joined with a cylinder surface defined over ∂F. Let P be a parametrization of ∂F (over an appropriate subset of $\mathbb{R}^5$), then we obtain with an additional parameter $v \geq h$ a parametrization (P, v) of this 6-dimensional cylindrical part.
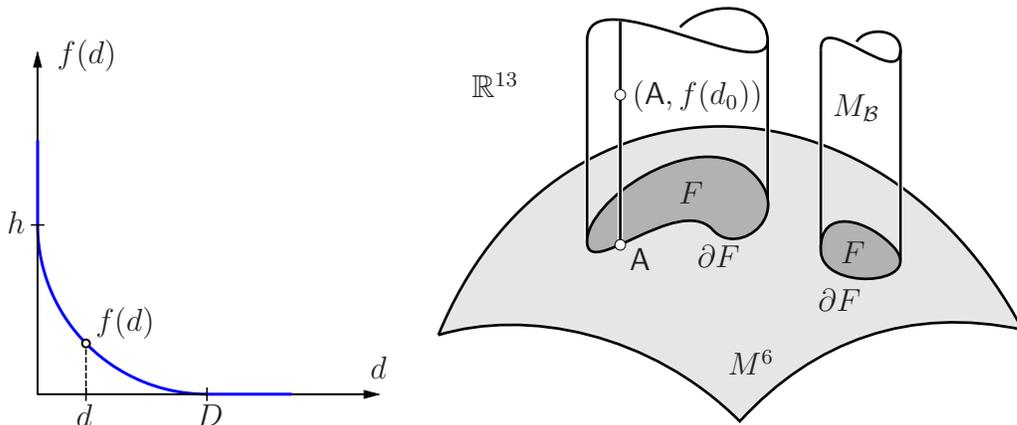
6

Fig. 3. (Left) Blending profile function $f(d)$. (Right) Forbidden region F with boundary ∂F and cylindric parts of barrier manifold $M_\mathcal{B}$.

3.2 Tangent Spaces of the Barrier Manifold

The tangent vector T at a position $\mathsf{A} = (\mathbf{a}_0, \ldots, \mathbf{a}_3)$ of M^6 is given by

$$\mathsf{T} = (\bar{\mathbf{c}} + \mathbf{c} \times \mathbf{a}_0, \mathbf{c} \times \mathbf{a}_1, \mathbf{c} \times \mathbf{a}_2, \mathbf{c} \times \mathbf{a}_3), \tag{1}$$

and has an interpretation as a velocity vector field $\mathbf{v}(\mathbf{x}) = \bar{\mathbf{c}} + \mathbf{c} \times \mathbf{x}$ in $\mathbb{R}^3$.

For the tangent space of the barrier manifold $M_\mathcal{B}$ we have the following three different cases:

Case 1: $d(\mathsf{A}) \geq D$. Equation (1) suffices to compute the tangent space of $M_\mathcal{B}$ for $d(\mathsf{A}) \geq D$; we just have to add a zero as 13-th coordinate.

Case 2: $0 < d(\mathsf{A}) < D$. This is the case of main interest. Let N_c be the common normal between $\alpha(\mathcal{B})$ and $\mathcal{O}$, along which the shortest distance $d_0 = d(\mathsf{A})$ occurs, see Fig. 4. N_c meets $\alpha(\mathcal{B})$ at a foot point $\mathbf{p}_f$. There, we consider two straight lines T_1, T_2 which are orthogonal to the contact normal N_c and thus tangent to the position $\alpha(\mathcal{B})$ of the body $\mathcal{B}$, see Fig. 4. We may assume orthogonal T_i's and then T_1, T_2, N_c define a Cartesian frame at the foot point $\mathbf{p}_f$. At first, we derive those tangent vectors of $M_\mathcal{B}$, whose 13-th coordinate is zero. These are characterized by vanishing directional derivative of the function d. Clearly, they belong to velocity fields of gliding motions along the offset $\tilde{\mathcal{O}}$ of $\mathcal{O}$ at distance d_0. Note that $\mathbf{p}_f$ is the contact point and N_c is the contact normal for such a gliding motion. By a well known result from kinematical geometry Pottmann and Wallner (2001), these velocity fields are characterized by an equation

$$\bar{\mathbf{n}}_c \cdot \mathbf{c} + \mathbf{n}_c \cdot \bar{\mathbf{c}} = 0. \tag{2}$$

Here, $(\mathbf{n}_c, \bar{\mathbf{n}}_c)$ are the Plücker coordinates of N_c. This says that the common normal N_c is contained in the linear complex of instantaneous path normals.
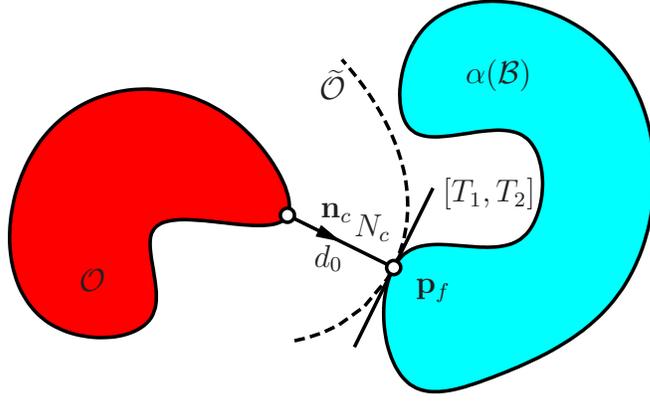
Fig. 4. Shortest distance d_0 between the moving body position $\alpha(\mathcal{B})$ and the obstacle $\mathcal{O}$.

It is easy to derive five independent velocity fields of gliding motions: We use instantaneous rotations about the three axes T_1, T_2, N_c and translations parallel to the two lines T_1, T_2. With $(\mathbf{t}_i, \bar{\mathbf{t}}_i)$ as Plücker coordinates of T_i, the corresponding velocity fields $(\mathbf{c}, \bar{\mathbf{c}})$ are

$$(\mathbf{c}_1, \bar{\mathbf{c}}_1) = (\mathbf{t}_1, \bar{\mathbf{t}}_1), \ (\mathbf{c}_2, \bar{\mathbf{c}}_2) = (\mathbf{t}_2, \bar{\mathbf{t}}_2), \ (\mathbf{c}_3, \bar{\mathbf{c}}_3) = (\mathbf{n}_c, \bar{\mathbf{n}}_c), \tag{3}$$

and

$$(\mathbf{c}_4, \bar{\mathbf{c}}_4) = (\mathbf{0}, \mathbf{t}_1), \ (\mathbf{c}_5, \bar{\mathbf{c}}_5) = (\mathbf{0}, \mathbf{t}_2). \tag{4}$$

To verify (2) for these velocity fields, one uses the condition $\bar{\mathbf{g}} \cdot \mathbf{h} + \mathbf{g} \cdot \bar{\mathbf{h}} = 0$ for two intersecting lines $G = (\mathbf{g}, \bar{\mathbf{g}})$ and $H = (\mathbf{h}, \bar{\mathbf{h}})$. Thus, we obtain with (1) five tangent vectors of $M_\mathcal{B}$ at the point $(\mathsf{A}, f(d(\mathsf{A})))$,

$$\mathsf{T}_i = (\bar{\mathbf{c}}_i + \mathbf{c}_i \times \mathbf{a}_0, \mathbf{c}_i \times \mathbf{a}_1, \mathbf{c}_i \times \mathbf{a}_2, \mathbf{c}_i \times \mathbf{a}_3, 0), \quad i = 1, \ldots, 5. \tag{5}$$

We assume that $\mathbf{n}_c$ is normalized and points outside the obstacle, i.e., in direction of increasing d. Displacing $\alpha(\mathcal{B})$ by a translation with vector $\lambda \mathbf{n}_c$ changes the distance value to $d_0 + \lambda$, since the contact normal remains the same for sufficiently small λ. In other words, $d(\mathsf{A}_\lambda) = d_0 + \lambda$ at $\mathsf{A}_\lambda = (\mathbf{a}_0 + \lambda \mathbf{n}_c, \mathbf{a}_1, \mathbf{a}_2, \mathbf{a}_3)$. This leads to a curve C in the barrier manifold, parameterized with help of λ,

$$\mathsf{C}(\lambda) = (\mathbf{a}_0 + \lambda \mathbf{n}_c, \mathbf{a}_1, \mathbf{a}_2, \mathbf{a}_3, f(d_0 + \lambda)). \tag{6}$$

The tangent of this curve at $\lambda = 0$ gives us the 6-th tangent vector,

$$\mathsf{T}_6 = (\mathbf{n}_c, \mathbf{0}, \mathbf{0}, \mathbf{0}, f'(d_0)). \tag{7}$$

Case 3: $d(\mathsf{A}) = 0$. To each point A in the boundary ∂F of the forbidden region, i.e., $d_0 = d(\mathsf{A}) = 0$, we have an infinite number of points in $M_\mathcal{B}$, namely in its cylindrical part, see Fig. 3. However, at all points of such a cylinder ruling, the

tangent space is the same. It is spanned by the five vectors (5) to instantaneous gliding motions of the body along the obstacle and by $(0, \ldots, 0, 1) \in \mathbb{R}^{13}$.

As mentioned earlier, one should not use a graph representation of the profile. If (t_1, t_2) is a tangent vector of the profile curve at d_0, i.e., (t_1, t_2) is parallel to $(1, f'(d_0))$, we use

$$\mathsf{T}_6 = (t_1 \mathbf{n}_c, \mathbf{0}, \mathbf{0}, \mathbf{0}, t_2). \tag{8}$$

This representation also holds for $d_0 = 0$, since then we have $(t_1, t_2) = (0, 1)$.

3.3 Projection Onto the Barrier Manifold

In the previous section we have derived basis vectors of the 6-dimensional tangent space at a point $(\mathsf{A}, f(d(\mathsf{A})))$ of the barrier manifold $M_{\mathcal{B}} \subset \mathbb{R}^{13}$. This allows us to compute the tangent space of the high-dimensional surface Φ used in Algorithm 1. Once we have computed the stepsize of the current iteration step, we apply the displacement in the tangent space of Φ. Then we need an admissible projection from a point in the tangent space of Φ onto Φ, see Fig. 1. One possibility is to perform the projection in the low-dimensional space for each position $\mathsf{A}_s \subset \mathbb{R}^{13}$ of the moving body separately. First we project the point A_s orthogonally onto M^6 by setting the 13-th coordinate equal to zero. The new translation of the Euclidean displacement in $\mathbb{R}^3$ is given by the first three coordinates of the point A_s, and the new rotation matrix in $\mathbb{R}^3$ is the best-fit orthogonal matrix to the affine matrix given by the 4-th till 12-th coordinate of A_s, computed with the methods presented in Hofer et al. (2004). Then we compute the distance of each new position of the moving body to the obstacle $\mathcal{O}$ to get the new 13-th coordinate, i.e., all together the new position on the barrier manifold $M_{\mathcal{B}}$. In case of penetration we translate the moving body position in direction of the common normal out of the obstacle.

Algorithm 2 (Variational motion design in the presence of obstacles) *The algorithm employs the following steps:*

(1) *Given are N collision free input positions $\mathcal{B}(u_j)$ at time instances u_j, obstacles $\mathcal{O}_i$, and an energy functional $E \in \{E_1, E_2, E_t\}$.*
(2) *Compute an obstacle avoiding energy-minimizing motion with the conservative algorithm of Hofer and Pottmann (2004):*
   (a) *Replace the moving body $\mathcal{B}$ by a minimum enclosing ball $\mathcal{B}_e$ with radius r centered in the barycenter $\mathbf{s}$ of $\mathcal{B}$.*
   (b) *Use Alg. 1 to compute the path of the barycenter $\mathbf{s}(u)$ such that it minimizes E and avoids the given obstacles with a minimum distance r. For details on computing such an obstacle avoiding curve we refer to Hofer and Pottmann (2004).*
   (c) *Separately minimize the energy of the rotational part of the motion*

using Alg. 1 (i.e., the energy E of a curve on the manifold $O(3)$ of orthogonal matrices, embedded in $\mathbb{R}^9$).

(3) The motion resulting of step 2 corresponds to a curve on M^6 that avoids the forbidden regions in a conservative way. We lift this curve onto the barrier manifold $M_{\mathcal{B}}$ and then employ Alg. 1. This results in an energy-minimizing rigid body motion $\mathcal{B}^*(u)$ that avoids the given rigid obstacles.

Remark 1 *In some cases, e.g. a narrow channel, the initial motion planned in a conservative way may not exist, since the bounding sphere of the moving body will not fit through the channel. However, a final solution can exist. Here one would benefit from a bump surface, which does not enforce the obstacles in such a strong way at the beginning of the iteration, cf. Fig. 13 in (Hofer and Pottmann, 2004). Geometrically this means that the curve on the barrier manifold can interfere with the obstacles at the beginning, but as the bump of the barrier manifold over the obstacles grows from a flat hill to a mountain with steeper and steeper walls, the curve is pushed out of the obstacles more and more.*

4 Experimental Results

We have implemented the algorithm in Matlab and tested it on a 1.8GHz personal computer. The examples illustrated in Fig. 5 have been computed using Alg. 2 and show open and cyclic motions that minimize the energy functional E_2:

(1) (Left) The unconstrained energy-minimizing rigid body motion corresponding to the point $\mathbf{p}$ in Alg. 1. Some of the obstacles are penetrated by this unconstrained motion.
(2) (Middle) The initial obstacle avoiding rigid body motion corresponding to the point $\mathbf{x}_0$ in Alg. 1.
(3) (Right) The constrained energy-minimizing rigid body motion corresponding to the point $\mathbf{p}^*$ in Alg. 1.

When we compare the open and the closed motion to the same input positions (right column in Fig. 5, the top two and the bottom two images) we can see that the overall shape of the motion is different, which goes along with what we expect to happen.

In our implementation, the computation time for all optimization parts is in sum a few seconds. The distance computations with the algorithms from the literature Arya et al. (1998); Tsai (2002); Zhao (2005) are a bit more time consuming.
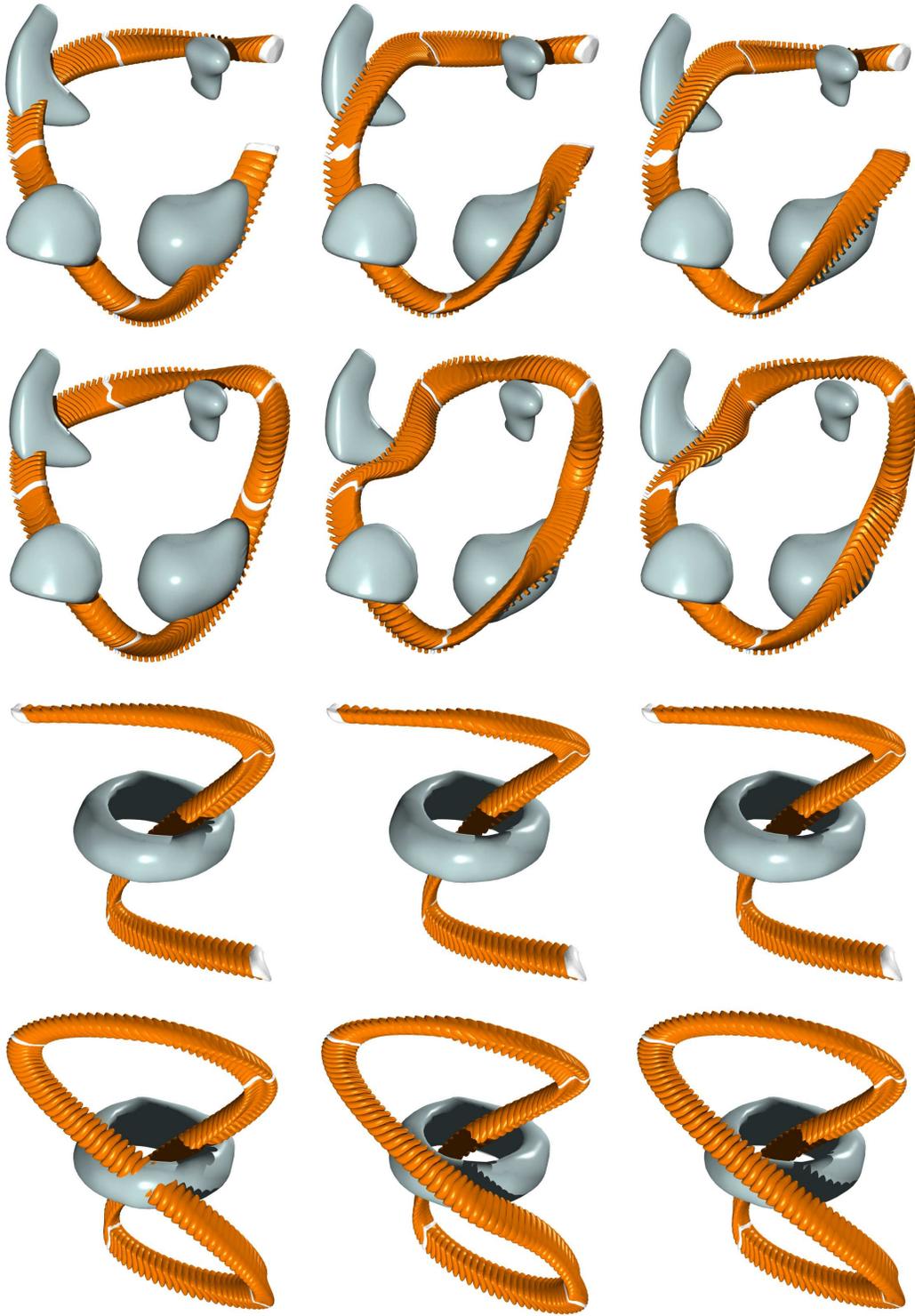
Fig. 5. (Left column) unconstrained minimizing motions, (Middle column) initial motions, (Right column) constrained minimum motions.
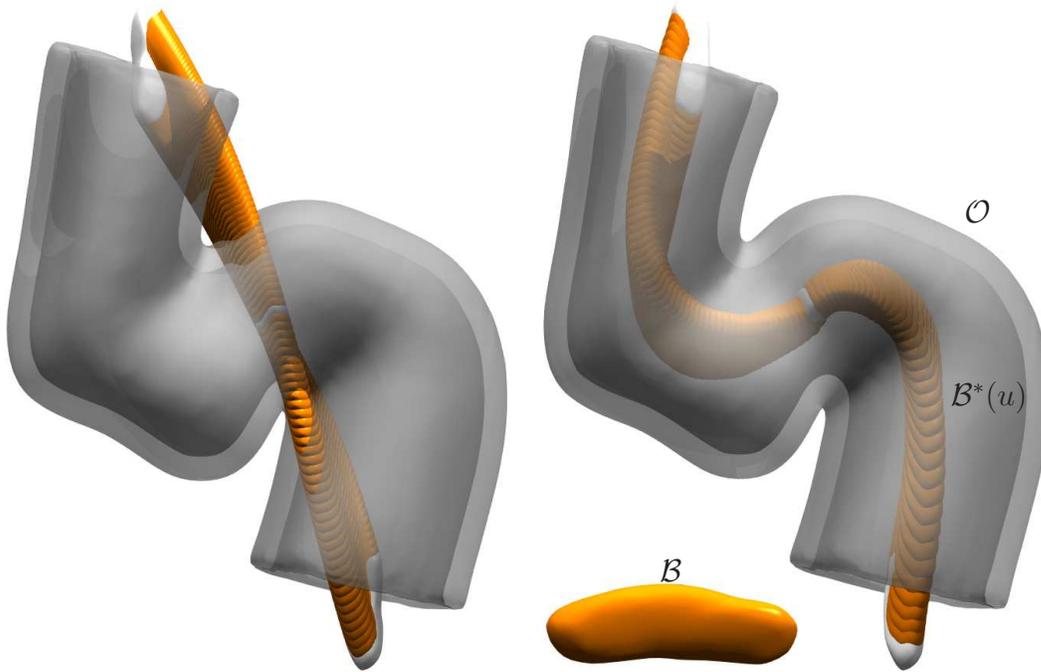
Fig. 6. Energy-minimizing motion of the cucumber shaped rigid body $\mathcal{B}$ (middle, bottom) passing through a narrow channel $\mathcal{O}$: (Left) The unconstrained minimizer clearly interferes with the obstacle. (Right) The constrained minimizer $\mathcal{B}^*(u)$ winds its way through the channel.

For the actual design of an energy-minimizing motion in the presence of obstacles the designer has the following parameters to influence the resulting rigid body motion, (i) the number of fixed positions that have to be interpolated, (ii) the number of intermediate positions (fineness of the motion), and (iii) the tension parameter τ in the energy functional E_τ.

The example shown in Fig. 6 shows a rigid body motion passing through a narrow channel. The rigid body is cucumber shaped (see Fig. 6 in the middle on the bottom) and the single obstacle is an S-shaped channel. We have chosen the linear parts of the three input positions as follows: in the first input position the moving body points into the entry hole of the channel, for the second input position we rotated the first input position through 90 degrees around a horizontal axis, and the third input position is obtained by rotating the second one again about the same axis about 90 degrees. The translational parts of the input positions have been chosen such that all three input positions do not interfere with the channel.

Since the bounding sphere of the moving body is too big to fit through the channel, we had to slightly modify step 2 of Alg. 2 and used an a bit relaxed condition to create an initial obstacle avoiding motion. Then we ran step 3 of Alg. 2 until we reached a local minimum of the energy functional. Note that we did set a distance threshold such that the moving body keeps a small

minimum distance to the obstacle.

For comparison reasons we show in Fig. 6 on the left the energy-minimizing motion that does not consider the channel as an obstacle. It can be clearly seen that this motion interferes with the obstacle. The obstacle avoiding motion that passes through the channel and minimizes the energy functional can be seen on the right in Fig. 6.

5 Conclusion

In this paper we give an answer to a question that remained open in our previous work (Hofer and Pottmann, 2004). In particular, we demonstrate how the geometric optimization algorithm of Hofer and Pottmann (2004) can be used to compute energy-minimizing rigid body motions in the presence of obstacles in a way such that all available degrees of freedom are actually employed. This not only improves the previously available conservative solution but also allows the computation of energy-minimizing rigid body motions in the presence of obstacles in situations where the conservative algorithm fails.

References

Arya, S., Mount, D. M., Netanyahu, N. S., Silverman, R., Wu, A. Y., 1998. An optimal algorithm for approximate nearest neighbor searching in fixed dimensions. J. ACM 45 (6), 891–923.

Azariadis, P. N., Aspragathos, N. A., 2005. Obstacle representation by bump-surfaces for optimal motion-planning. Robotics and Autonomous Systems 51, 129–150.

Barr, A. H., Currin, B., Gabriel, S., Hughes, J. F., 1992. Smooth interpolation of orientations with angular velocity constraints using quaternions. In: Proceedings of ACM SIGGRAPH 92. ACM Press / ACM SIGGRAPH, pp. 313–320.

Bohl, H., 1999. Kurven minimaler Energie auf getrimmten Flächen. Ph.D. thesis, Univ. Stuttgart.

Choset, H., Lynch, K. M., Hutchinson, S., Kantor, G., Burgard, W., Kavraki, L. E., Thrun, S., 2005. Principles of Robot Motion: Theory, Algorithms, and Implementations. The MIT Press.

de Berg, M., van Kreveld, M., Overmars, M., Schwarzkopf, O., 2000. Computational Geometry, 2nd Edition. Springer.

Hofer, M., Pottmann, H., 2004. Energy-minimizing splines in manifolds. ACM Transactions on Graphics (Proceedings of ACM SIGGRAPH) 23 (3), 284–293.

Hofer, M., Pottmann, H., Ravani, B., 2004. From curve design algorithms to the design of rigid body motions. The Visual Computer 20 (5), 279–297.

Jüttler, B., Wagner, M., 2002. Kinematics and animation. In: Farin, G., Kim, M. S., Hoschek, J. (Eds.), Handbook of Computer Aided Geometric Design. Elsevier, pp. 723–748.

Latombe, J. C., 2001. Robot Motion Planning, 6th Edition. Kluwer.

Meek, D. S., Ong, B. H., Walton, D. J., 2003. Constrained interpolation with rational cubics. Computer-Aided Design 20, 253–275.

Myles, A., Peters, J., 2005. Threading splines through 3D channels. Computer-Aided Design 37, 139–148.

Opfer, G., Oberle, H. J., 1988. The derivation of cubic splines with obstacles by methods of optimization and optimal control. Numer. Math. 52, 17–31.

Pottmann, H., Wallner, J., 2001. Computational Line Geometry. Mathematics + Visualization. Springer, Heidelberg.

Ramamoorthi, R., Barr, A., 1997. Fast construction of accurate quaternion splines. In: Proceedings of ACM SIGGRAPH 1997. ACM Press / ACM SIGGRAPH, New York, pp. 287–292.

Shoemake, K., 1985. Animating rotation with quaternion curves. In: Proceedings of ACM SIGGRAPH 85. Vol. 19 of Computer Graphics. pp. 245–254.

Tsai, R., 2002. Rapid and accurate computation of the distance function using grids. J. Comput. Phys. 178(1), 175–195.

Zhao, H.-K., 2005. A fast sweeping method for eikonal equations. Math. Comp. 74(250):603–627.